

# Metadata of the chapter that will be visualized online

Chapter Title	Non-colloidal Nanocatalysts Fabricated with Nanolithography and Arc Plasma Deposition	
Copyright Year	2013	
Copyright Holder	Springer Science+Business Media New York	
Corresponding Author	Family Name	<b>Kim</b>
	Particle	
	Given Name	<b>Sang Hoon</b>
	Suffix	
	Division	Center for Materials Architecturing
	Organization	Korea Institute of Science and Technology (KIST)
	Address	Seoul, 136-791, Republic of Korea
	Division	School of Science
	Organization	University of Science and Technology (UST)
	Address	Daejeon, 305-333, Republic of Korea
Author	Family Name	<b>Park</b>
	Particle	
	Given Name	<b>Jeong Young</b>
	Suffix	
	Division	Graduate School of EEWS (WCU) and NanoCentury KI
	Organization	Korea Advanced Institute of Science and Technology (KAIST)
	Address	Daejeon, Republic of Korea
	Division	Center for Nanomaterials and Chemical Reactions
	Organization	Institute for Basic Science
	Address	Daejeon, 305-701, Republic of Korea
Abstract	<p>In this chapter, we discuss the most recent advances in the preparation of nanocatalysts via dry processes. We describe the fabrication of metal nanoparticles using lithography and the synthesis of catalytic nanoparticles using non-colloidal techniques, including plasma deposition and lithographical techniques. Synthesis of oxide-supported metal catalysts via wet-chemical processes is well known in heterogeneous catalysis [1–3]. Impregnation, coprecipitation, deposition-precipitation, ion exchange, sol–gel, and colloidal processes are typical examples of wet processes. Typically, precursors of the active catalyst materials are dissolved and reacted in an aqueous or organic solution and the solution is mixed with ceramic supports to prepare the</p>	

oxide-supported metal catalysts. In general, the wet-chemically produced oxide-supported metal catalysts need to undergo annealing processes at elevated temperature in order to eliminate the organic materials required for the wet processes, such as solvent, surfactant, or capping agents [4–6]. The annealing process can cause oxidation of the catalyst metal particles, causing catalytic activity deterioration. In order to overcome the shortcomings of wet-chemical processes, direct vaporization of metallic materials to deposit active materials on ceramic supports has drawn considerable interest due to its simplicity, high reproducibility, and the possibility for large-scale production. Examples of such dry synthesis processes for nanocatalyst production are arc plasma deposition (APD) [7–9], e-beam lithography [10, 11], and laser vaporization [12, 13]. In this chapter, we introduce APD and nanolithography technologies for preparing catalyst materials and discuss recent advances in their application.

---

# Chapter 3

## Non-colloidal Nanocatalysts Fabricated with Nanolithography and Arc Plasma Deposition

Sang Hoon Kim and Jeong Young Park

### 3.1 Introduction

In this chapter, we discuss the most recent advances in the preparation of nanocatalysts via dry processes. We describe the fabrication of metal nanoparticles using lithography and the synthesis of catalytic nanoparticles using non-colloidal techniques, including plasma deposition and lithographical techniques. Synthesis of oxide-supported metal catalysts via wet-chemical processes is well known in heterogeneous catalysis [1–3]. Impregnation, coprecipitation, deposition-precipitation, ion exchange, sol–gel, and colloidal processes are typical examples of wet processes. Typically, precursors of the active catalyst materials are dissolved and reacted in an aqueous or organic solution and the solution is mixed with ceramic supports to prepare the oxide-supported metal catalysts. In general, the wet-chemically produced oxide-supported metal catalysts need to undergo annealing processes at elevated temperature in order to eliminate the organic materials required for the wet processes, such as solvent, surfactant, or capping agents [4–6]. The annealing process can cause oxidation of the catalyst metal particles, causing catalytic activity deterioration. In order to overcome the shortcomings of wet-chemical processes, direct vaporization of metallic materials to deposit active materials on ceramic

---

S.H. Kim (✉)

Center for Materials Architecturing, Korea Institute of Science and Technology (KIST),  
Seoul 136-791, Republic of Korea

School of Science, University of Science and Technology (UST), Daejeon 305-333,  
Republic of Korea

e-mail: kim\_sh@kist.re.kr

J.Y. Park

Graduate School of EEWS (WCU) and NanoCentury KI, Korea Advanced Institute  
of Science and Technology (KAIST), Daejeon, Republic of Korea

Center for Nanomaterials and Chemical Reactions, Institute for Basic Science,  
Daejeon 305-701, Republic of Korea

J.Y. Park (ed.), *Current Trends of Surface Science and Catalysis*,

DOI 10.1007/978-1-4614-8742-5\_3, © Springer Science+Business Media New York 2013

supports has drawn considerable interest due to its simplicity, high reproducibility, and the possibility for large-scale production. Examples of such dry synthesis processes for nanocatalyst production are arc plasma deposition (APD) [7–9], e-beam lithography [10, 11], and laser vaporization [12, 13]. In this chapter, we introduce APD and nanolithography technologies for preparing catalyst materials and discuss recent advances in their application.

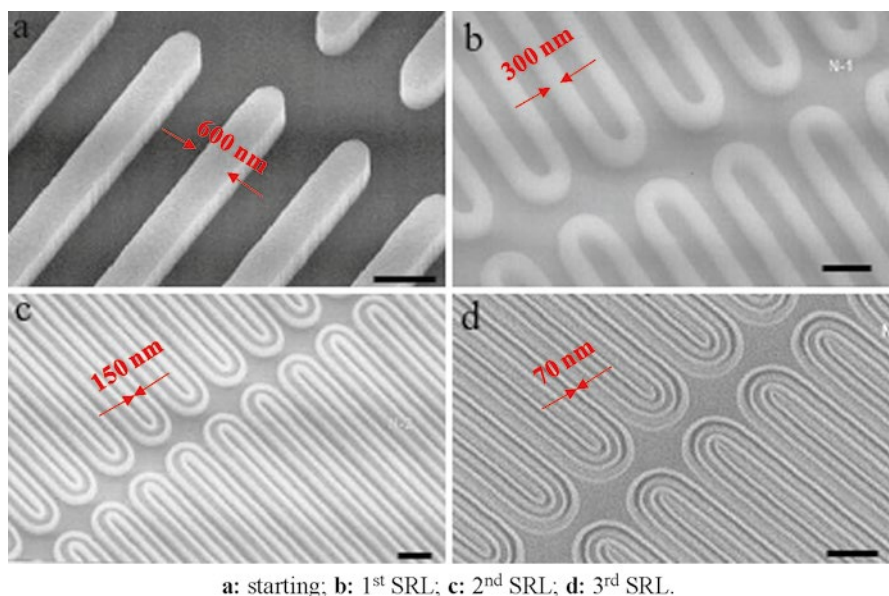
## 3.2 Nanocatalysts Fabricated with Lithography

### 3.2.1 Nanolithography for Fabrication of Nanodots and Nanowires

Lithography-based nanocatalyst fabrication is one of the main techniques developed for the production of catalysts with high throughput [14–16]. It has the advantage of precise control of particle size and inter-particle distance. The two-dimensional (2D) array of nanocatalysts produced via lithography is also highly monodispersed. Lithography-based nanocatalysts can be formed on any substrate; therefore, it can form a controlled oxide–metal interface, which offers opportunities for studying the role of the interface between the catalytically active phase and the support in catalytic reactions. Moreover, a fabricated 2D array of nanodots or nanowires can be easily cleaned and crystallized for catalyst studies with various surface treatments.

Most importantly, the nanolithography routes exemplified in this section are applicable to the fabrication of any other 2D nanocatalysts on different substrates. The simplest route is electron beam lithography (EBL) [17–19], which utilizes high-resolution pattern writing with a focused electron beam, followed by electron-sensitive resist/etching. It can fabricate nanoparticles with a size of ~10 nm. However, nanofabrication with EBL is limited by low throughput and high cost. A new method called size reduction lithography (SRL) [20] can reduce the mold from 0.6  $\mu\text{m}$  polysilicon to ~7 nm silicon nanowire. The nanowire pattern is transferred into polymethyl methacrylate (PMMA) under high pressure and high temperature using nano imprint lithography (NIL). A thermal oxide layer formed by oxygen-plasma etching upon the residual PMMA is then removed. In this way, a nanoscale mold is fabricated. Figure 3.1 presents the multiplication of pattern density by SRL. Pt atoms can be deposited by electron beam evaporation to form Pt nanowires. Thermal treatment in vacuum, hydrogen, or oxygen crystallizes the Pt nanowires [21, 22]. The major contaminant, carbon from PMMA, can be removed by thermal oxidation under low pressure ( $1 \times 10^{-6}$  Torr) of  $\text{NO}_2$  at 573 K. The adsorbed oxygen remaining after the carbon removal step can be removed by converting CO into  $\text{CO}_2$ .

Another method for fabricating catalytic nanodots is called mold-to-mold cross imprint (MTMCI) [24]. This technique is capable of producing high areal density nanodots of any metal on any surface. It includes three main steps. First, a silicon



a: starting; b: 1<sup>st</sup> SRL; c: 2<sup>nd</sup> SRL; d: 3<sup>rd</sup> SRL.

**Fig. 3.1** Multiplication of pattern density by size reduction lithography. (a) After patterning a sacrificial poly-Si layer; (b) after SiO<sub>2</sub> deposition, a SiO<sub>2</sub> spacer etch by CF<sub>4</sub> plasma, and removal of the sacrificial poly-Si by KOH; (c) after poly-Si deposition, poly-Si spacer etch by Cl<sub>2</sub> and HBr, and removal of SiO<sub>2</sub> by HF; and (d) after SiO<sub>2</sub> deposition, SiO<sub>2</sub> spacer etch by CF<sub>4</sub> plasma, and removal of sacrificial poly-Si by KOH. Thus, 8 (=23) lines with a line width of 70 nm and interline spacing of 80 nm were generated after threefold reduction lithography. The scale bars in all images are 1  $\mu$ m. Reprinted with permission from ref. [23]. Copyright Springer

wire mold is fabricated using spacer lithography. Second, a MTMCI technique is used to convert the silicon spacer nanowires into silicon nanopillars. The principle of the second step is to pattern a silicon spacer nanowire mold with another nanowire mold by imprinting one mold placed perpendicularly onto the other. Figure 3.2a shows the protocol for the fabrication of a silicon nanodot model using the MTMCI technique. In the second step, an array of silicon nanopillars is fabricated at the intersection of the silicon and chromium nanowires by etching the silicon. The silicon nanopillars thus formed have a size of 15  $\times$  30  $\times$  250 nm. Figure 3.2b is an array of silicon nanopillars, which acts as the final mold for the fabrication of the 2D catalytic nanodots on the substrate. The third step is the imprinting of the Pt nanodots (Fig. 3.3). The silicon nanopillar mold is imprinted into a PMMA layer on silicon oxide layers formed naturally on a commercially available silicon wafer. A thin layer of Cr is deposited via angled evaporation as a hard mask for the PMMA mold. Then, Pt atoms are deposited into the uncovered nanowell, forming Pt nanodots with dimensions of 15  $\times$  30  $\times$  5 nm. Figure 3.2c is an array of Pt nanodots on silicon oxide after removal of the residual PMMA. Compared to the cleaning and crystallization of Pt nanowires fabricated through SRL, similar cleaning routes [21, 22] are used for cleaning and crystallization of the Pt nanodots.

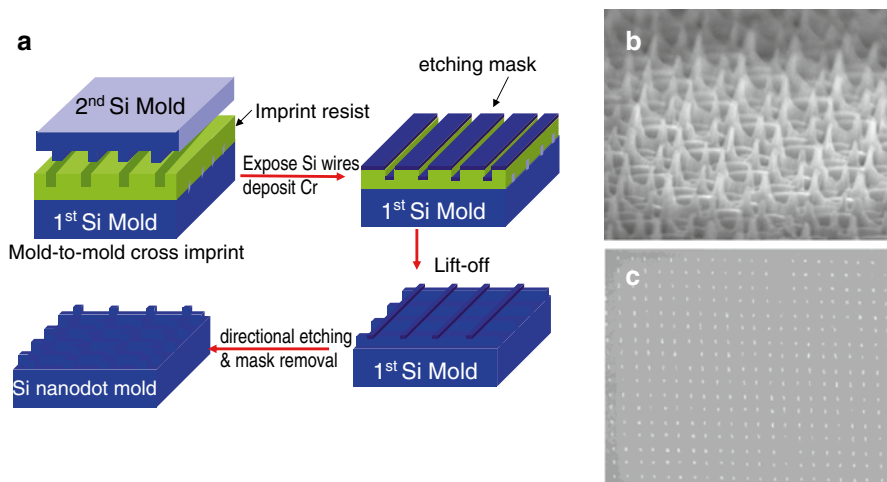
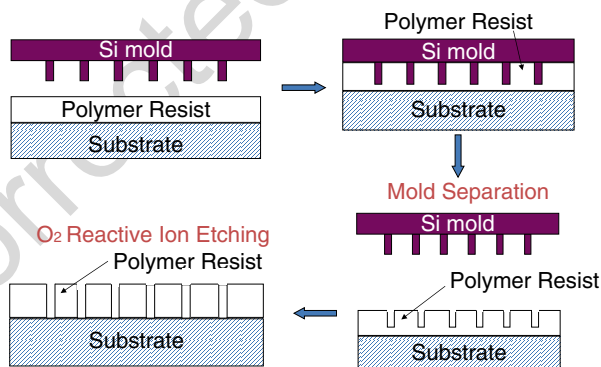


**Fig. 3.2** (a) Scheme of mold-to-mold cross imprint (MTMCI) to fabricate a nanopillar mold. (b) SEM of a nanopillar mold (each nanopillar:  $15 \times 30 \times 250$  nm). (c) A homogeneous array of Pt nanodots (each nanodot:  $15 \times 30 \times 5$  nm) made by MTMCI. Reprinted with permission from ref. [23]. Copyright Springer

this figure will be printed in

**Fig. 3.3** Scheme of nanoimprint lithography. Reprinted with permission from ref. [23]. Copyright Springer



### 3.2.2 Catalytic Properties of Nanowires Fabricated with Lithography

Dense arrays of platinum nanowires deposited on the oxide thin-film surfaces of  $\text{ZrO}_2$ ,  $\text{SiO}_2$ ,  $\text{Al}_2\text{O}_3$ , and  $\text{CeO}_2$  are fabricated by combining lithographic nanofabrication and nanoimprint technology [16]. These nanowire arrays have been used to study the effects of oxide support on the catalytic oxidation of CO. Figure 3.4 shows

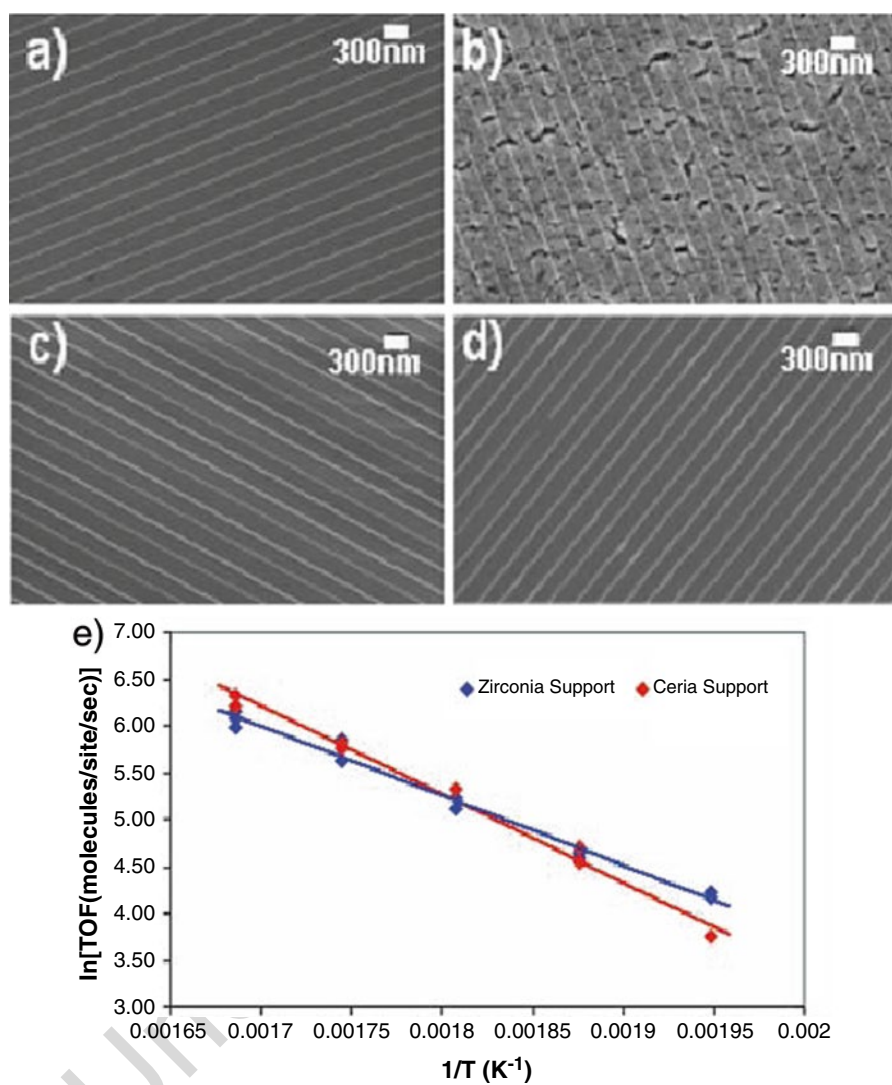


**Fig. 3.4** SEM images of 20-nm wide Pt nanowires on different oxide supports. All wires are 5 nm in height. (a) Silica support; (b) ceria support; (c) alumina support; (d) zirconia support. (e) Arrhenius plots measured for CO oxidation reactions on zirconia- and ceria-supported Pt nanowire arrays. Reprinted with permission from ref. [16]. Copyright Springer

SEM images of the nanowire arrays on different oxides. From the SEM images, the typical dimensions of a single platinum nanowire are  $20 \times 5 \times 12$  nm (width  $\times$  height  $\times$  length). Catalytic oxidation of CO to  $\text{CO}_2$  over the various catalyst arrays was carried out in temperatures of 513–613 K. Figure 3.4e shows Arrhenius plots for the reaction on zirconia- and ceria-supported samples. Apparent activation

86  
87  
88  
89  
90

energies for the zirconia- and ceria-supported wire arrays are  $14.6 \pm 0.2$  and  $18.8 \pm 0.2$  kcal/mol, respectively. The nanowires on silica have an activation energy of  $12.6 \pm 0.2$  kcal/mol. Therefore, the nanocatalysts composed of metal nanowires and oxide supports reveal support dependence for both reaction turnover frequency (TOF) and the measured activation energy.

### 3.3 Nanocatalysts Fabricated Via Arc Plasma Deposition

#### 3.3.1 Introduction to Arc Plasma Deposition

APD, or cathodic arc deposition, has been traditionally applied when preparing dense thin films of corrosion-resistant, protective, and decorative coatings, such as TiN, TiC, and CrN [25–27]. This method is usually regarded as physical vapor deposition (PVD), but it differs from other PVD methods in that energetic plasma ions condense to form dense films in APD, while in other PVD methods, it is the vapor of neutral atoms that condense [25].

In APD, very high current densities ( $\sim 10^{12}$  A/m<sup>2</sup>) let the cathode material directly evaporate from the surface. A plasma discharge then generates cathodic arcs within the vapor. The size of arc spot is typically a few microns [26]. The plasma generated at arc spots expands rapidly into the ambient vacuum. The final velocities of the generated ions are  $\sim 1\text{--}2 \times 10^4$  m/s and are largely independent of the cathode materials. These velocities correspond to the kinetic energies of about 20 eV for light elements and 200 eV for heavy elements [25]. The biggest obstacle of implementing the APD method has been that macrodroplets are also emitted simultaneously from the cathode spot along with the plasma ions and electrons. The droplets adhere to the film and act as defects. Another problem of the APD method is that it is not easy to control the arc generation location [28, 29]. In order to reduce or eliminate macrodroplets, various methods have been tried, such as steered arc [30], distributed arc [31], and filters [28, 32, 33].

Among these trials, pulsed coaxial APD offers macrodroplet-free plasma deposition without large-scale conventional magnetic filter systems in the vacuum chamber. Chun et al. developed the pulsed coaxial APD system shown in Fig. 3.5a [34]. A high-voltage pulse (a few kilovolts, tens of microseconds) is applied between the trigger and cathode cylinder. This voltage induces dielectric breakdown and trigger discharge. Then, the main discharge occurs sequentially between the cathode spot and the cylindrical anode, where a voltage of 50–300 V is applied. During arc discharge, a very large current ( $\sim 2,000$  A) flows through the cathode (Fig. 3.5b). Due to the large magnetic field induced by the current, plasma ions and electrons fly away from the cathode towards the substrate. Meanwhile, any macrodroplets, which are neutral, fly towards the anode and adhere to the anode surface. Because the duration of the arc is less than 1 ms, heating of the cathode material and generation of macrodroplets are minimized. As the arc plasma is generated between the cathode



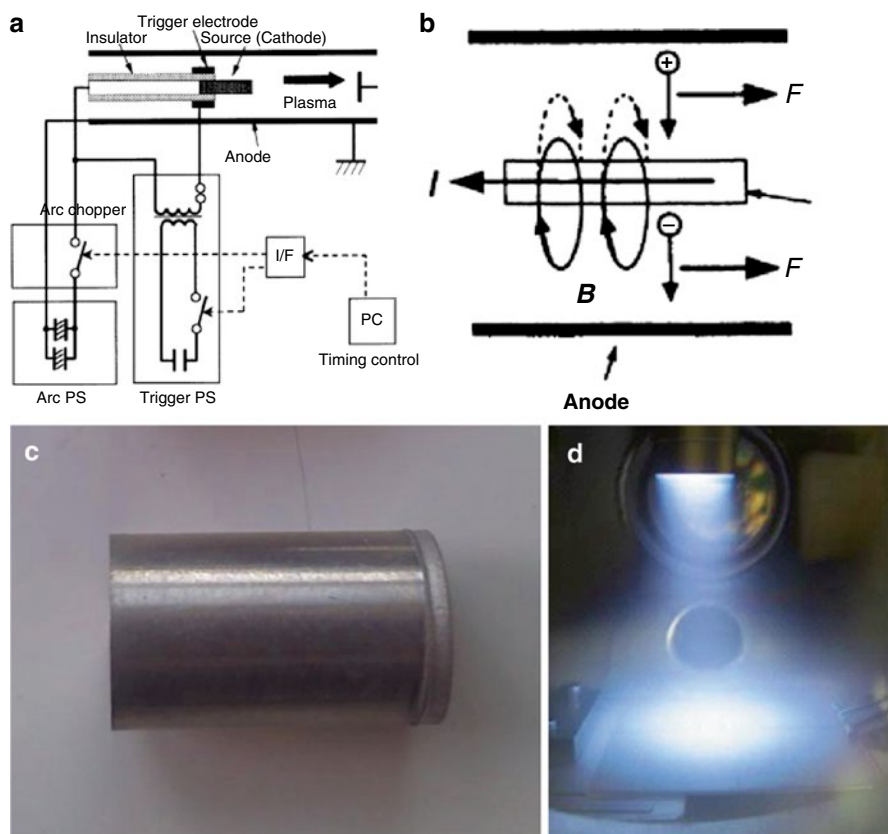


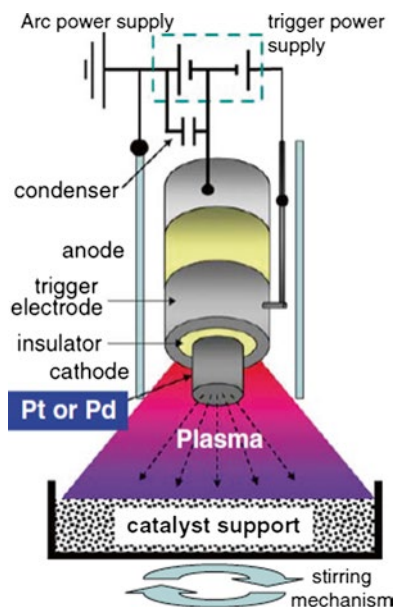
**Fig. 3.5** Schematic diagram of (a) coaxial pulsed arc plasma deposition system and (b) quasi-stationary model of a generated arc plasma.  $I$  is the arc current,  $B$  is the magnetic field induced by  $I$ , and  $F$  is the electromagnetic force applied to the plasma ions and electrons. Reprinted with permission from ref. [34]. Copyright 2000 Elsevier Science S.A. (c) Used cathode cylinder made of palladium. The plasma is generated from the circular rim on the right side. (d) A generated arc plasma. The plasma beam accelerates towards bottom of the image. Courtesy of Ulvac-Riko, Inc.

and anode surfaces, arc spots are limited to the protruded rim of the cathode cylinder. For example, a slightly used cathode cylinder is shown in Fig. 3.5c. In the figure, the rim on the right is used for plasma generation. Therefore, by controlling the length of the protrusion, arc spots can be limited to the rim of the protrusion. Figure 3.5d shows an actual arc plasma beam generated from the cathode (top). The accelerated plasma beam hits the bottom, where catalyst support materials are placed. In the case of powder-type catalyst supports, the powder is constantly stirred for effective dispersion of the deposited catalyst nanoparticles on the powder. In case of thin-film-type catalyst supports, no stirring is needed.

This pulsed coaxial APD has been used to fabricate multilayer structures with sub-nanometer thickness control [34–36] without the need of filters, such as curved

**Fig. 3.6** Schematic of arc plasma deposition of nanoparticles on a catalyst support.

In the case of powder-type catalyst supports, the powder is constantly stirred for effective dispersion. In the case of thin-film-type catalyst supports, no stirring is needed. Reprinted with permission from ref. [38]. Copyright 2009 Springer Science + Business media, LLC

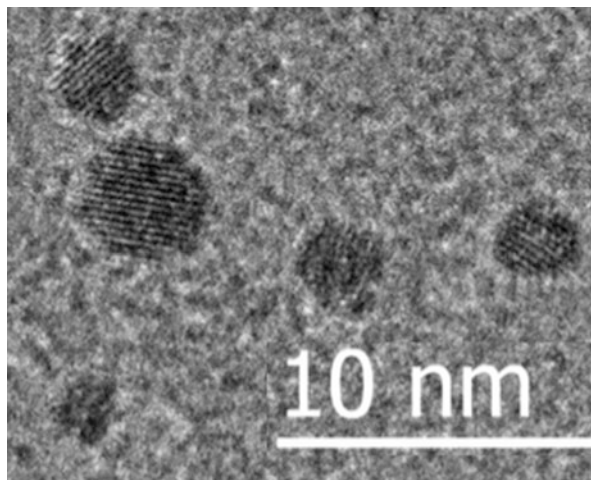


ducts, to remove macrodroplets [37]. Another advantage of pulsed coaxial APD is that each pulse generates a very large number of nanoparticle ions a few nanometer in size ( $\sim 1\text{--}5$  nm). The amount of deposited materials or, for the two-dimensional case, coverage of the deposited materials can be easily controlled by the number of pulses.

As long as the material is solid and can be formed as a cylindrical cathode target for an APD system, any material can be dry-deposited as nanoparticles without going through wet-chemical processes. Those deposited nanoparticles can be used as seed particles for growing nanotubes [39, 40] or for decorating underlying nanostructures to form complex nanocomposites with enhanced functionalities [41]. Among these new possibilities, using APD to dry deposit nanoparticles as nanocatalyst materials have drawn significant attention and interest is rapidly growing [42]. Figure 3.6 shows a schematic of depositing catalytic nanoparticles on catalyst supports. It is a dry process in a high vacuum chamber with a base pressure of  $\sim 10^{-7}$  Torr. Nanoparticles generated from the cathode surface are accelerated towards the bottom due to the high magnetic field induced by the high current flowing along the cathode axis, as discussed above.

Figure 3.7 shows a TEM image of individual Pt nanoparticles deposited by APD on an amorphous carbon film substrate. The dark dots are Pt nanoparticles and the gray background is the amorphous carbon substrate. The nanoparticles are  $\sim 1\text{--}5$  nm in size and lattice structures are clearly seen in the particles. In the following sections, recent applications of APD for nanocatalyst preparation are discussed.

**Fig. 3.7** Arc plasma-deposited Pt nanoparticles on amorphous carbon



### 3.3.2 Nanocatalysts on Two-Dimensional Supports Using APD

163

As a model for metal-oxide hybrid catalysts using strong metal-support interactions (SMSI) [43], thin-film-type substrates have been employed to disperse catalyst nanoparticles [44–46]. Recently, Qadir et al. compared the catalytic activity of Pt nanoparticles prepared by conventional wet-chemistry methods and by APD on TiO<sub>2</sub> thin film substrates [9]. In the study, ~150 nm thick TiO<sub>2</sub> films were sputtered on Si wafers and used as catalytic supports. Approximately the same amount of Pt (0.12 mg) was deposited using APD (150 pulses, arc discharge voltage 100 V, discharge condenser capacity 1,080 μF) and conventional impregnation. For impregnation, potassium hexachloroplatinate (K<sub>2</sub>PtCl<sub>6</sub>) was dissolved in distilled water and droplets were dropped and dried, then the sample was annealed at 500 °C for 5 h to remove organic substances. The catalytic activity was tested using CO oxidation in an ultra-high-vacuum (UHV) batch reactor. As can be seen in Fig. 3.8, the catalytic activity of the dry-deposited Pt nanoparticles on the TiO<sub>2</sub> films was higher than that of the impregnated ones. The 150-pulse APD Pt was enough to have 100 % surface coverage. Therefore, it was assumed that the deposited Pt is thicker than one monolayer and that the layer is flat. From these assumptions, the number of active sites on the deposited Pt layer was calculated, and the turnover frequency (TOF) (Fig. 3.8a) and activation barrier for the reaction (Fig. 3.8b) were measured.

Still, it is not easy to find clues for the observed difference in catalytic activities from only these structural aspects. The XPS analysis in Fig. 3.9 shows that the impregnated and annealed Pt nanoparticles have inactive bulk oxide states, while the APD Pt nanoparticles are purely metallic. This oxide formation during annealing is considered the main reason for the difference in the catalytic activities. In order to improve catalytic activity, impregnated and annealed Pt nanoparticles on TiO<sub>2</sub> films were reduced under 100 Torr of hydrogen at 250 °C for 1 h to decrease the oxidation state. However, the catalytic activity after reduction was still lower than that of the

164

165

166

167

168

169

170

171

172

173

174

175

176

177

178

179

180

181

182

183

184

185

186

187

188

189

this figure will be printed in b/w

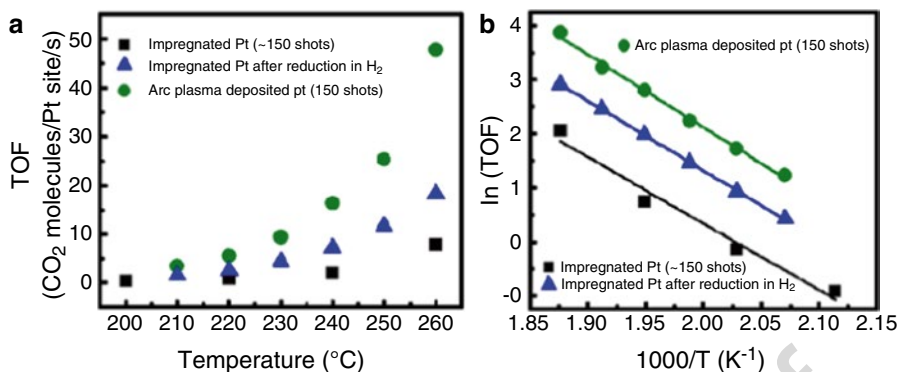


**Fig. 3.8** Comparison of the catalytic activity of Pt nanoparticles on TiO<sub>2</sub> films prepared by APD and impregnation. Reprinted with permission from ref. [9]. Copyright 2012 American Chemical Society

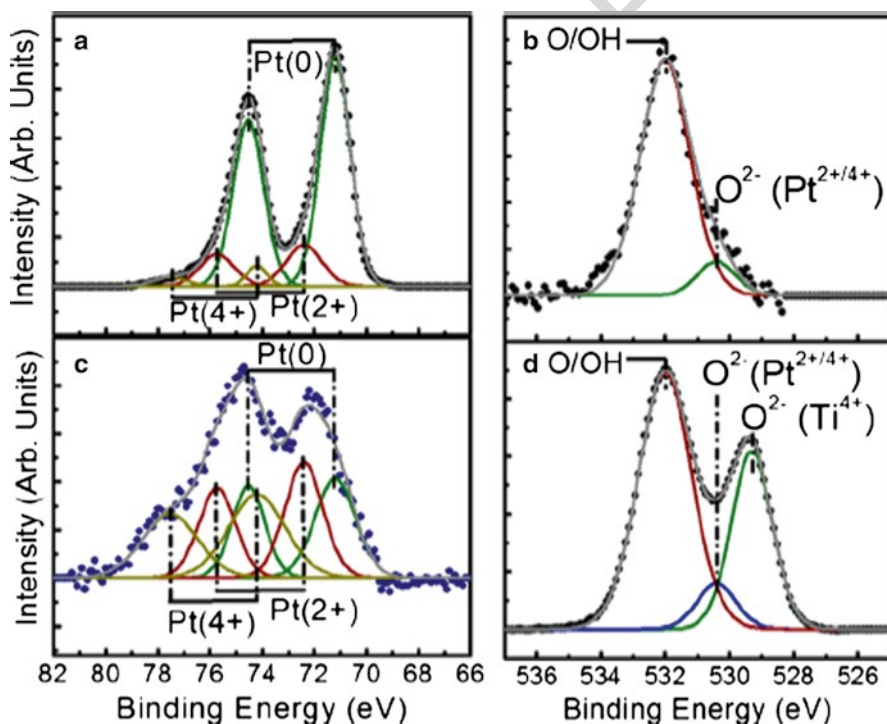
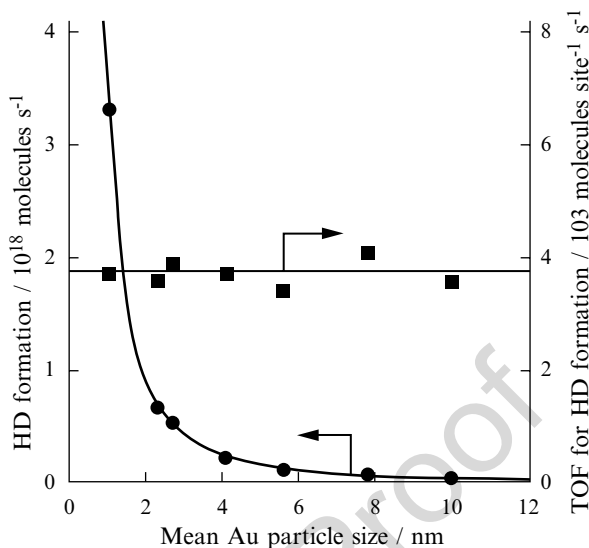


**Fig. 3.9** XPS measurement of (a) Pt 4f and (b) O 1s peaks of 150 pulse APD Pt nanoparticles and (c) Pt 4f and (d) O 1s peaks of a similar amount of impregnated and annealed Pt nanoparticles on TiO<sub>2</sub> films. Reprinted with permission from ref. [9]. Copyright 2012 American Chemical Society

**Fig. 3.10** Comparison of the HD formation rates vs. mean gold particle size for the same amount of deposited gold on TiO<sub>2</sub>(110). Reprinted with permission from ref. [47]. Copyright 2009 Wiley-VCH Verlag



APD Pt nanoparticles (Fig. 3.9a). Furthermore, XPS survey spectra showed a very small peak for K on the impregnated Pt nanoparticles. The presence of K ion may have blocked active sites too [9]. This study showed that APD enabled the deposition of metallic Pt nanoparticles on TiO<sub>2</sub> films with neither oxidation due to annealing nor impurities commonly found in conventional wet-chemical processes.

Fujitani et al. examined hydrogen molecule dissociation at low temperature (425 K) on gold nanoparticles deposited on TiO<sub>2</sub>(110) single crystal surface via APD [47]. In the study, they deposited the same amount of gold nanoparticles with average diameters of ~1–10 nm by changing the discharge condenser capacity between 360 and 2,200  $\mu$ F. They then exposed the prepared Au/TiO<sub>2</sub>(110) surface to the H<sub>2</sub> and D<sub>2</sub> exchange reaction and measured the rate of HD formation (Fig. 3.10). The rate of HD formation increased dramatically when the gold particle size was below 2 nm, while the TOF was more or less constant over the entire particle size range. TOFs were calculated by dividing the number of HD molecules formed per second by the total number of gold atoms at the periphery of the gold particles. Based on this measurement, the active sites for H<sub>2</sub> dissociation are along the periphery around the deposited gold particles. This study shows that it is possible to control the size of nanoparticles generated by APD in the nanometer range by controlling the parameters for arc plasma generation.

### 3.3.3 Nanocatalysts on Three-Dimensional Supports Using APD

For a two-dimensional substrate, we can assume the number of active sites or directly measure the coverage of catalyst particles. Therefore, quantitative analysis



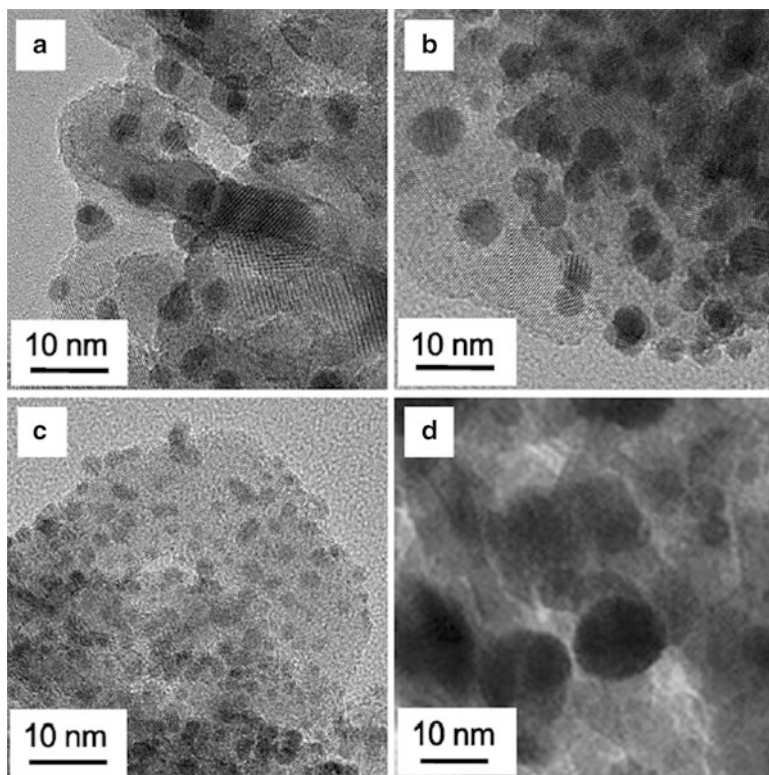


**Fig. 3.11** TEM images of APD-deposited gold and platinum nanoparticles on TiO<sub>2</sub> powder. The arc discharge condenser capacity was 1,800  $\mu$ F. (a) Au/TiO<sub>2</sub> at discharge voltage of 200 V, (b) Au/TiO<sub>2</sub> at discharge voltage of 300 V, (c) Pt/TiO<sub>2</sub> at discharge voltage of 200 V, and (d) Au/TiO<sub>2</sub> prepared by sol-gel method for comparison. Reprinted with permission from ref. [8]. Copyright 2013 Elsevier Science S.A.

(e.g., TOF and active barrier calculations) is possible, as shown in the previous section, and two-dimensional substrates can be used as model catalyst supports. On the other hand, three-dimensional powder supports are much more widely used in industry, but it is not easy to do quantitative analysis using a powder support. Still, it is important to improve processes to incorporate catalyst nanoparticles on powder support, such as better dispersion of ever smaller nanoparticles or controlling the adhesion strength between catalytic nanoparticles and support powder materials. Recently, Kim et al. studied the catalytic activity of nanometer-sized Au and Pt particles deposited on TiO<sub>2</sub> powder via APD [8]. In the study, they controlled the size of the deposited nanoparticles by changing the arc discharge voltage,  $V$ , for generating plasma. Figures 3.11 and 3.12 show TEM images and the size distribution of the APD-deposited Au and Pt nanoparticles on TiO<sub>2</sub> powder, respectively. The metallic nanoparticles are seen as dark spots, while the catalyst support TiO<sub>2</sub> powder particles are seen as bright and extended shapes. Nanoparticles deposited by

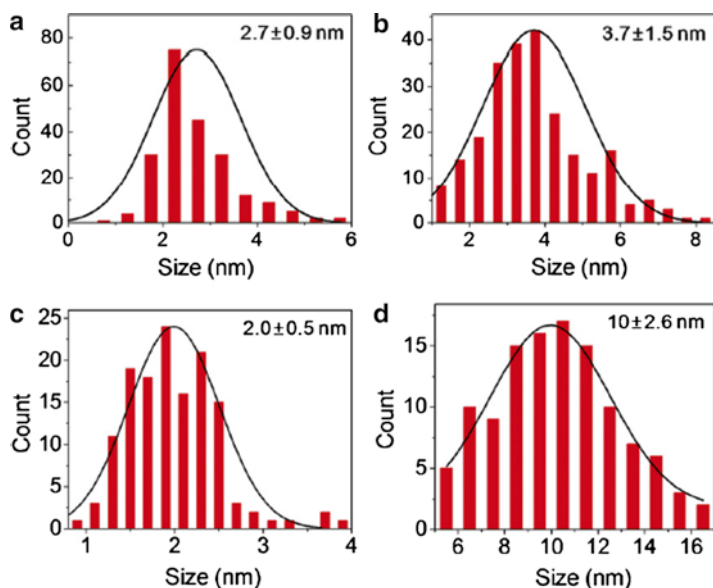


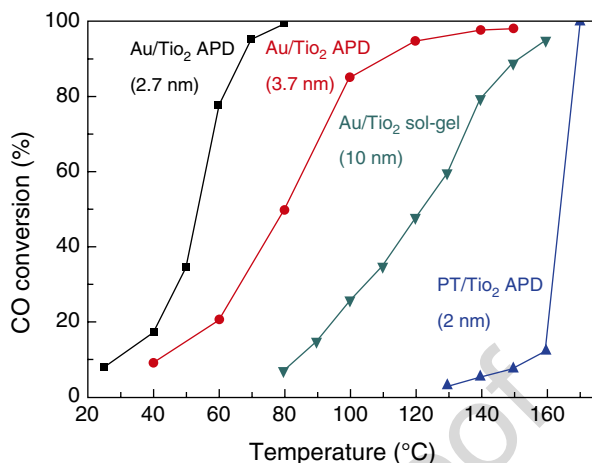
**Fig. 3.12** Particle size distributions of the Au/TiO<sub>2</sub> and Pt/TiO<sub>2</sub> particles shown in Fig. 3.9. (a)–(d) corresponds to those in Fig. 3.9. Reprinted with permission from ref. [8]. Copyright 2013 Elsevier Science S.A.

APD tend to increase in size with increasing  $V$ ; this tendency can be seen in Fig. 3.11a, b. Although prepared using the same deposition conditions, the Au and Pt nanoparticles had different sizes (Fig. 3.11a, c). Figure 3.11d shows nanoparticles prepared using the wet-chemical sol–gel method for comparison. The sol–gel-prepared nanoparticles are ~10 nm in size—bigger than those prepared by APD, which are ~2–4 nm in size (Fig. 3.12).

Gold nanoparticles are well known for their high catalytic activity for CO oxidation [48, 49]. On the nanometer scale, the catalytic activity of gold nanoparticles increases with decreasing size [41, 50]. On the other hand, it is known that the catalytic activity of Pt nanoparticles is independent of particle size [49, 51]. The catalytic activity comparison for the samples shown in Fig. 3.13 reflects these tendencies. In the comparison, the overall CO oxidation efficiency followed the order of Au/TiO<sub>2</sub> 200 V > Au/TiO<sub>2</sub> 300 V > Au/TiO<sub>2</sub> sol–gel > Pt/TiO<sub>2</sub> 200 V. Regardless of preparation method, be it dry or wet, particle size is the most important parameter for the catalytic activity of nano-sized gold. On the other hand, Pt/TiO<sub>2</sub> 200 V had the lowest catalytic activity, as the catalytic activity was not very different from that of bulk Pt. The catalytic activity of gold increased with decreasing particle size and eventually surpassed Pt. Again, it was possible to control the size of the nanoparticles with the parameters for generating the arc plasma. However, it was within the same materials only. For different materials, the particles differed in size when using the same parameters for arc plasma generation.

this figure will be printed in b/w

**Fig. 3.13** Catalytic activity comparison for Au/TiO<sub>2</sub> and Pt/TiO<sub>2</sub>. Reprinted with permission from ref. [8]. Copyright 2013 Elsevier Science S.A.



Hinokuma et al. reported a similar study on dispersing Pt and Pd nanoparticles on  $\gamma$ -alumina powder using APD and conventional impregnation. They compared the catalytic activities for CO oxidation [38]. In the study, they found out that the average size of the Pt nanoparticles deposited by APD is  $\sim 2.5$  nm and the size of the Pd nanoparticles is 6.8 nm. XPS measurements showed that the Pt nanoparticles were metallic regardless of the preparation method. As for the Pd nanoparticles, they were mostly in their oxide form (PdO) when prepared by impregnation. When prepared by APD, however, the metallic Pd had a higher fraction (60 %) than the Pd-oxide (40 %). As the APD process occurs in vacuum and directly vaporizes the metallic cathode materials, the deposited nanoparticles tend to be metallic. Figure 3.14 shows a comparison of the catalytic activities of Pt/alumina and Pd/alumina powders prepared by APD and impregnation. For comparison, they loaded the same amount (0.4 wt%) of Pt and Pd on  $\gamma$ -alumina powder and labeled “apg” for APD preparation and “imp” for impregnation. For the Pt/alumina samples, APD-prepared samples showed higher catalytic activity than impregnation-prepared samples due to their higher dispersion (Fig. 3.14a, left). However, after thermal aging in 10 % H<sub>2</sub>O/air at 900 °C for 25 h, deactivation was more pronounced for the APD-prepared samples than for the impregnation-prepared sample (Fig. 3.14b, left). This observation indicates that the thermal stability of APD-dispersed Pt nanoparticles on  $\gamma$ -alumina is not so good. With TEM, they actually observed sintering of Pt nanoparticles up to 20 nm in size. For the Pd/alumina samples, the situation was somewhat different. The APD-prepared samples showed a slightly lower catalytic activity than the impregnation-prepared samples (Fig. 3.14a, right). They explained this difference by the higher catalytic activity of PdO than metallic Pd [52].

Hinokuma et al. continued their study to include prepared bimetallic Pd-Fe nanoparticles on ceria powder using APD and investigated their catalytic activity for CO oxidation [53]. In the study, they prepared bimetallic nanoparticles using two plasma guns in a chamber, one for Pd and one for Fe. They prepared the



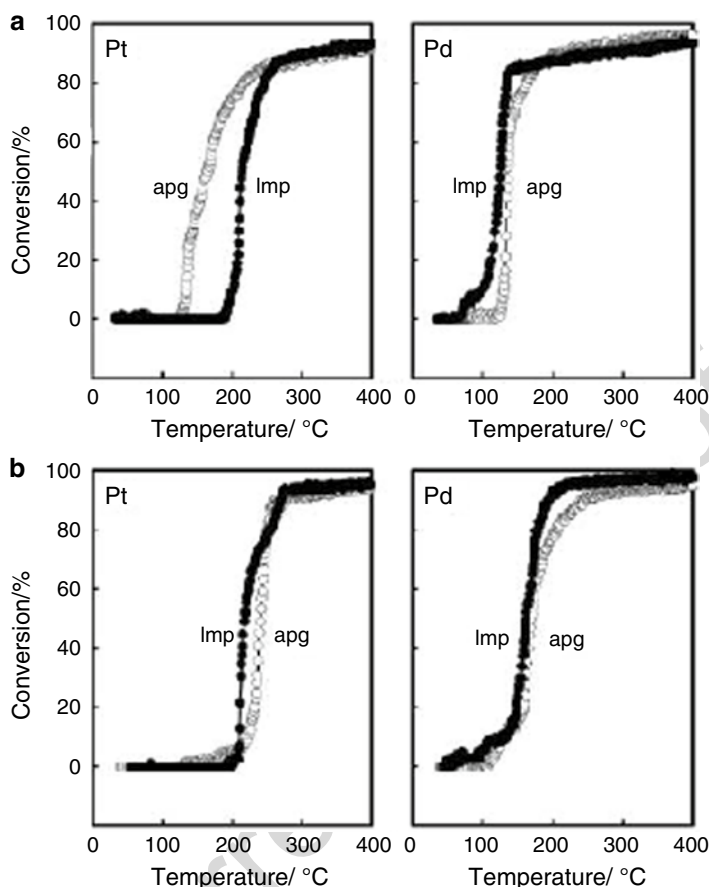


**Fig. 3.14** Catalytic activity comparison for Pt/alumina and Pd/alumina (a) as prepared and (b) after thermal aging. Reprinted with permission from ref. [38]. Copyright 2009 Springer Science+Business media, LLC

bimetallic nanoparticles using the two cathode guns synchronously (syn) and asynchronously (asyn). Synchronous pulses of Pd and Fe resulted in Pd-Fe bimetallic alloy nanoparticles, while asynchronous pulses resulted in individual Pd and Fe nanoparticles on the ceria support. They found out that Pd-Fe bimetallic nanoparticles showed slightly higher catalytic activity than the individual metal nanoparticles (Fig. 3.15a). They attributed these findings to better dispersion and a higher metallic fraction of Pd in the Pd-Fe alloy nanoparticles on ceria. The catalytic activity increased after thermal aging for both the synchronous- and asynchronous-prepared samples (Fig. 3.15b). The authors argued that, in contrast to the alumina case above, thermal aging helped stabilize the Pd–O–Ce bonding, keeping the dispersion of nanoparticles intact, which enabled higher catalytic activity after thermal aging [54].

276  
277  
278  
279  
280  
281  
282  
283  
284  
285  
286  
287

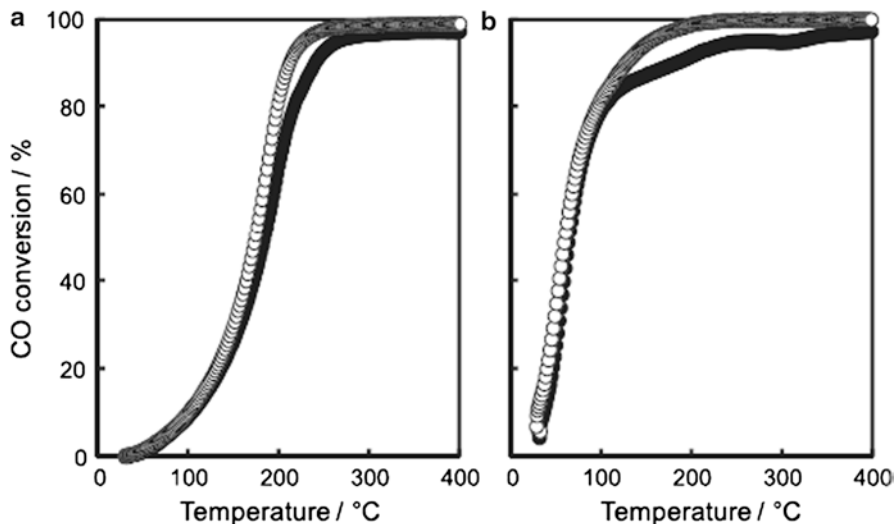


**Fig. 3.15** Comparison of catalytic activity for Pd-Fe on ceria powder by APD. (*Open circles*) Pd-Fe/ceria (syn) (*filled circles*) Pd-Fe/ceria (asyn), (**a**) before and (**b**) after thermal aging. Reprinted with permission from ref. [53]. Copyright 2013 Elsevier Science S.A.

### 3.3.4 Some New Applications for Nanoparticles Prepared Via APD

Other than the familiar gas-phase catalytic reactions, examples of APD-deposited nanoparticle applications in some new fields are also emerging. In order to investigate photocatalytic antibacterial effects, Oveisi et al. deposited silver nanoparticles on mesoporous anatase titania films using APD [55]. The size of the deposited nanoparticles ranged between 3.7 and 5.6 nm by changing the number of arc plasma pulses. When a droplet of *E. coli* suspension is dropped on top of Ag nanoparticles dispersed on titania and irradiated with UV light, the survival fraction of *E. coli* cells decreased as the nanoparticle size decreased. In other words, smaller Ag nanoparticles were more effective for inactivating the bacteria. For sensing applications, Ito et al. reported detection of hydrogen peroxide using APD-deposited Pt nanoparticles on carbon electrodes in an electrochemical setup [56]. In the study, they varied the coverage of the Pt nanoparticles on glassy carbon surfaces by incrementally increasing the number of plasma pulses from 5 to 20. The average particle size was 2.7 nm. After annealing the Pt-deposited glassy carbon, only the Pt nanoparticles deposited using five APD pulses remained as individual particles, while Pt particles deposited using more APD pulses coalesced to form connected island shapes. After annealing, electrodes with individual Pt nanoparticles showed better sensitivity than electrodes with connected Pt islands for hydrogen peroxide detection.

### 3.4 Summary and Outlook

309

In this chapter, we have discussed the most recent advances in the preparation of catalyst nanoparticles on catalyst support using dry processes. These two-dimensional model catalyst arrays fabricated using nanolithography have been used to study the support dependence of CO oxidation reaction kinetics; they indicate that the most important factor affecting TOF is the interaction of the platinum and the support. The APD method was traditionally used for preparation of dense protective coating layers. However, with the advent of pulsed APD, new applications for preparing metallic nanoparticles in a direct and dry process are emerging. So far, applications are limited to the much studied gas-phase reactions—mostly the model CO oxidation reaction. However, we have also noticed that the scope of applications is widening, too (e.g., liquid-phase photocatalysts, electrode materials for fuel cells and secondary batteries, and sensor applications). The biggest advantage of APD is that it is relatively easy to generate a large amount of particles a few nanometer in size. It is also easy to control the size of the generated nanoparticles, on the nanometer scale, by controlling APD parameters, such as the number of arc plasma pulse shots, arc discharge voltage, and arc discharge condenser capacitance. As for substrates for deposition, the APD method provides a simple and easy method for direct and dry deposition of metallic nanoparticles on a variety of substrates, such as two-dimensional thin films and three-dimensional powders. Therefore, the possibilities for new applications are enormous. We assume that more attention will be paid to this method with respect to generating dry nanoparticles for many new applications with the central focus remaining catalyst materials.

**Acknowledgments** This work was supported by a grant from the future R&D Program funded by the Korea Institute of Science and Technology (2E23900). This work was supported by the WCU (World Class University) program (31-2008-000-10055-0 and 2012R1A2A1A01009249) through the National Research Foundation, the Research Center Program (CA1201) of IBS (Institute for Basic Science), and from the Fundamental R&D Program for Core Technology of Materials funded by the Ministry of Knowledge Economy, Republic of Korea.

### References

338

1. Ertl G, Knozinger H, Weitkamp J (1999) Preparation of solid catalysts. Wiley-VCH, Weinheim
2. Regalbuto JR (2007) Handbook of catalyst preparation. Taylor & Francis, Boca Raton
3. Somorjai GA, Park JY (2008) Colloid science of metal nanoparticle catalysts in 2D and 3D structures. Challenges of nucleation, growth, composition, particle shape, size control and their influence on activity and selectivity. Top Catal 49:126–135
4. Park J, Aliaga C, Renzas JR, Lee H, Somorjai G (2009) The role of organic capping layers of platinum nanoparticles in catalytic activity of CO oxidation. Catal Lett 129:1–6
5. Kuhn JN, Tsung C-K, Huang W, Somorjai GA (2009) Effect of organic capping layers over monodisperse platinum nanoparticles upon activity for ethylene hydrogenation and carbon monoxide oxidation. J Catal 265:209–215

6. Aliaga C, Park JY, Yamada Y, Lee HS, Tsung CK, Yang P, Somorjai GA (2009) Sum frequency generation and catalytic reaction studies of the removal of organic capping agents from Pt nanoparticles by UV-ozone treatment. *J Phys Chem C* 113:6150–6155
7. Agawa Y, Endo S, Matsuura M, Ishii Y (2010) Multi-functional materials and structures III, Pts 1 and 2, vol 123–125. Advanced materials research. Trans Tech Publications, Switzerland, pp 1067–1070
8. Kim SH, Jung C-H, Sahu N, Park D, Yun JY, Ha H, Park JY (2013) Catalytic activity of Au/TiO<sub>2</sub> and Pt/TiO<sub>2</sub> nanocatalysts prepared with arc plasma deposition under CO oxidation. *Appl Catal Gen* 454:53–58
9. Qadir K, Kim SH, Kim SM, Ha H, Park JY (2012) Support effect of arc plasma deposited Pt nanoparticles/TiO<sub>2</sub> substrate on catalytic activity of CO oxidation. *J Phys Chem C* 116: 24054–24059
10. Komanicky V, Iddir H, Chang K-C, Menzel A, Karapetrov G, Hennessy D, Zapol P, You H (2009) Shape-dependent activity of platinum array catalyst. *J Am Chem Soc* 131:5732–5733
11. Tsirlin T, Zhu J, Grunes J, Somorjai G (2002) AFM and TEM studies of Pt nanoparticle arrays supported on alumina model catalyst prepared by electron beam lithography. *Top Catal* 19: 165–170
12. Glaspell G, Hassan HMA, Elzatahry A, Abdalsayed V, Samy El-Shall M (2008) Nanocatalysis on supported oxides for CO oxidation. *Top Catal* 47:22–31
13. Yang Y, Saoud KM, Abdelsayed V, Glaspell G, Deevi S, El-Shall MS (2006) Vapor phase synthesis of supported Pd, Au, and unsupported bimetallic nanoparticle catalysts for CO oxidation. *Catal Commun* 7:281–284
14. Contreras AM, Grunes J, Yan XM, Liddle A, Somorjai GA (2005) Fabrication of platinum nanoparticles and nanowires by electron beam lithography (EBL) and nanoimprint lithography (NIL): comparison of ethylene hydrogenation kinetics. *Catal Lett* 100:115–124
15. Contreras AM, Grunes J, Yan XM, Liddle A, Somorjai GA (2006) Fabrication of 2-dimensional platinum nanocatalyst arrays by electron beam lithography: ethylene hydrogenation and CO-poisoning reaction studies. *Top Catal* 39:123–129
16. Contreras AM, Yan XM, Kwon S, Bokor J, Somorjai GA (2006) Catalytic CO oxidation reaction studies on lithographically fabricated platinum nanowire arrays with different oxide supports. *Catal Lett* 111:5–13
17. Jacobs PW, Ribeiro FH, Somorjai GA, Wind SJ (1996) New model catalysts: uniform platinum cluster arrays produced by electron beam lithography. *Catal Lett* 37:131–136
18. Jacobs PW, Wind SJ, Ribeiro FH, Somorjai GA (1997) Nanometer size platinum particle arrays: catalytic and surface chemical properties. *Surf Sci* 372:L249–L253
19. Yan XM, Contreras AM, Koebel MM, Liddle JA, Somorjai GA (2005) Parallel fabrication of sub-50-nm uniformly sized nanoparticles by deposition through a patterned silicon nitride nanostencil. *Nano Lett* 5:1129–1134
20. Yan XM, Kwon S, Contreras AM, Koebel MM, Bokor J, Somorjai GA (2005) Fabrication of dense arrays of platinum nanowires on silica, alumina, zirconia and ceria surfaces as 2-D model catalysts. *Catal Lett* 105:127–132
21. Grunes J, Zhu J, Anderson EA, Somorjai GA (2002) Ethylene hydrogenation over platinum nanoparticle array model catalysts fabricated by electron beam lithography: determination of active metal surface area. *J Phys Chem B* 106:11463–11468
22. Grunes J, Zhu J, Yang MC, Somorjai GA (2003) CO poisoning of ethylene hydrogenation over Pt catalysts: a comparison of Pt(111) single crystal and Pt nanoparticle activities. *Catal Lett* 86:157–161
23. Somorjai GA, Tao F, Park JY (2008) The nanoscience revolution: merging of colloid science, catalysis and nanoelectronics. *Top Catal* 47:1–14
24. Kwon S, Yan XM, Contreras AM, Liddle JA, Somorjai GA, Bokor J (2005) Fabrication of metallic nanodots in large-area arrays by mold-to-mold cross imprinting (MTMCI). *Nano Lett* 5:2557–2562
25. Anders A (2008) Cathodic arcs: from fractal spots to energetic condensation. Springer, New York

[AU1]

26. Randhawa H (1988) Cathodic arc plasma deposition technology. *Thin Solid Films* 167: 175–185 403
27. Randhawa H, Johnson PC (1987) A review of cathodic arc plasma deposition processes and their applications. *Surf Coat Technol* 31:303–318 405
28. Sanders DM, Anders A (2000) Review of cathodic arc deposition technology at the start of the new millennium. *Surf Coat Technol* 133:78–90 407
29. Takikawa H, Tanoue H (2007) Review of cathodic arc deposition for preparing droplet-free thin films. *IEEE Trans Plasma Sci* 35:992–999 409
30. Swift PD (1996) Macroparticles in films deposited by steered cathodic arc. *J Phys D: Appl Phys* 29:2025–2031 411
31. Shinno H, Fukutomi M, Fujitsuka M, Okada M (1985) In situ coating of low-z materials by reactive vacuum arc-deposition with a stabilized arc cathode. *J Nucl Mater* 133:749–753 413
32. Anders A (1999) Approaches to rid cathodic arc plasmas of macro- and nanoparticles: a review. *Surf Coat Technol* 120:319–330 415
33. Martin PJ, Bendavid A (2001) Review of the filtered vacuum arc process and materials deposition. *Thin Solid Films* 394:1–15 417
34. Chun S-Y, Chayahara A (2000) Pulsed vacuum arc deposition of multilayers in the nanometer range. *Surf Coat Technol* 132:217–221 419
35. Chun SY, Chayahara A (2000) Enhanced interfacial roughness in metallic multilayers prepared by pulsed cathodic arc deposition. *Surf Coat Technol* 127:282–284 421
36. Chun SY, Chayahara A, Posselt M (2004) Limitations on ultra-thin multilayers: pulsed cathodic arc and computer simulation. *Surf Coat Technol* 182:171–174 423
37. Li LH, Lu QY, Fu RKY, Chu PK (2008) Thickness uniformity and surface morphology of Fe, Ti, and Hf films produced by filtered pulsed cathodic arc deposition. *Surf Coat Technol* 203:887–892 425
38. Hinokuma S, Murakami K, Uemura K, Matsuda M, Ikeue K, Tsukahara N, Machida M (2009) Arc plasma processing of Pt and Pd catalysts supported on gamma-Al<sub>2</sub>O<sub>3</sub> powders. *Top Catal* 52:2108–2111 428
- [AU2] 39. Hiramatsu M, Nagao H, Taniguchi M, Amano H, Ando Y, Hori M (2005) High-rate growth of films of dense, aligned double-walled carbon nanotubes using microwave plasma-enhanced chemical vapor deposition. *Jpn J Appl Phys Part 2—Lett Express Lett* 44:L693–L695 431
40. Phokharatkul D, Ohno Y, Nakano H, Kishimoto S, Mizutani T (2008) High-density horizontally aligned growth of carbon nanotubes with CO nanoparticles deposited by arc-discharge plasma method. *Appl Phys Lett* 93:053112–053113 432
41. Chen JH, Lu GH (2006) Controlled decoration of carbon nanotubes with nanoparticles. *Nanotechnology* 17:2891–2894 433
- [AU3] 42. Takei T, Akita T, Nakamura I, Fujitani T, Okumura M, Okazaki K, Huang J, Ishida T, Haruta M (2012). In: Gates Bruce C, Jentoft Friederike C (eds) *Advances in catalysis*, vol 55. Academic, pp 1–126 434
- [AU4] 43. Haller GL, Resasco DE (1989) Metal-support interaction: group VIII metals and reducible oxides. *Adv Catal* 36:173–235 435
44. Belton DN, Sun YM, White JM (1986) Chemisorption of CO, NO, and H<sub>2</sub> on transition metal-titania thin film model catalysts. *J Catal* 102:338–347 436
45. Grunwaldt J-D, Baiker A (1999) Gold/titania interfaces and their role in carbon monoxide oxidation. *J Phys Chem B* 103:1002–1012 437
46. Hayek K, Fuchs M, Klötzer B, Reichl W, Rupprechter G (2000) Studies of metal—support interactions with “real” and “inverted” model systems: reactions of CO and small hydrocarbons with hydrogen on noble metals in contact with oxides. *Top Catal* 13:55–66 438
47. Fujitani T, Nakamura I, Akita T, Okumura M, Haruta M (2009) Hydrogen dissociation by gold clusters. *Angew Chem Int Ed* 48:9515–9518 439
48. Valden M, Lai X, Goodman DW (1998) Onset of catalytic activity of gold clusters on titania with the appearance of nonmetallic properties. *Science* 281:1647–1650 440
49. Haruta M (2002) Catalysis of gold nanoparticles deposited on metal oxides. *CATTECH* 6:102–115 441

50. Anpo M, Onaka M, Yamashita H (2003) Science and technology in catalysis 2002: proceedings of the fourth Tokyo conference on advanced catalytic science and technology, Kodansha, Tokyo, 14–19 July 2002
51. Boronat M, Corma A (2010) Origin of the different activity and selectivity toward hydrogenation of single metal Au and Pt on TiO<sub>2</sub> and bimetallic Au-Pt/TiO<sub>2</sub> catalysts. *Langmuir* 26:16607–16614
52. Farrauto RJ, Hobson MC, Kennelly T, Waterman EM (1992) Catalytic chemistry of supported palladium for combustion of methane. *Appl Catal Gen* 81:227–237
53. Hinokuma S, Katsuhara Y, Ando E, Ikeue K, Machida M (2013) Pd-Fe/CeO<sub>2</sub> bimetal catalysts prepared by dual arc-plasma deposition. *Catal Today* 201:92–97
54. Hinokuma S, Fujii H, Okamoto M, Ikeue K, Machida M (2010) Metallic Pd nanoparticles formed by Pd-O-Ce interaction: a reason for sintering-induced activation for CO oxidation. *Chem Mater* 22:6183–6190
55. Oveisi H, Rahighi S, Jiang XF, Agawa Y, Beitollahi A, Wakatsuki S, Yamauchi Y (2011) Improved inactivation effect of bacteria: fabrication of mesoporous anatase films with fine Ag nanoparticles prepared by coaxial vacuum arc deposition. *Chem Lett* 40:420–422
56. Ito T, Kunimatsu M, Kaneko S, Hirabayashi Y, Soga M, Agawa Y, Suzuki K (2012) High performance of hydrogen peroxide detection using Pt nanoparticles-dispersed carbon electrode prepared by pulsed arc plasma deposition. *Talanta* 99:865–870

# Author Queries

Chapter No.: 3      0002030075

Queries	Details Required	Author's Response
AU1	Please check if the edit made to ref. [7] is ok as edited.	
AU2	Please check the journal title for reference 39.	
AU3	Please provide chapter title and publisher location for reference 42.	
AU4	Please check if the inserted article title and journal title are correct.	